

Discovery of extended structures around two evolved planetary nebulae M 2–55 and Abell 2

Chih-Hao Hsia (夏志浩)¹, Yong Zhang (张泳)², Xi-Liang Zhang (张西亮)³ and Tao Luo (骆韬)¹

¹ State Key Laboratory of Lunar and Planetary Sciences, Macau University of Science and Technology, Taipa, Macau, China; chhsia@must.edu.mo

² School of Physics and Astronomy, Sun Yat-Sen University Zhuhai Campus, Tangjia, Zhuhai 519082, China; zhangyong5@mail.sysu.edu.cn

³ Yunnan Observatories, Chinese Academy of Sciences, Kunming 650216, China

Received 2019 December 11; accepted 2020 March 4

Abstract We report a multi-wavelength study of two evolved planetary nebulae (PNs) M 2–55 and Abell 2. Deep optical narrow-band images ([O III], H α , and [N II]) of M 2–55 reveal two pairs of bipolar lobes and a new faint arc-like structure. This arc-shaped filament around M 2–55 appears as a well-defined boundary from southwest to southeast, strongly suggesting that this nebula is in interaction with its surrounding interstellar medium. From the imaging data of *Wide-field Infrared Survey Explorer* (WISE) all-sky survey, we discovered extensive mid-infrared halos around these PNs, which are approximately twice the size of their main nebulae seen in the visible. We also present a mid-resolution optical spectrum of M 2–55, which shows that it is a high-excitation evolved PN with a low electron density of 250 cm⁻³. Furthermore, we investigate the properties of these nebulae from their spectral energy distributions (SEDs) by means of archival data.

Key words: infrared: ISM — ISM: structure — planetary nebulae: individual (M 2–55 and Abell 2) — stars: AGB and post-AGB

1 INTRODUCTION

As descendants of asymptotic giant branch (AGB) stars, planetary nebulae (PNs) are important objects to understand galactic abundance distribution and the ending of stellar evolution of low- and intermediate-mass stars. When the infrared (IR) technique was first developed, the PN NGC 7027 was found to have a strong excess in the IR, far above the continuum level expected from thermal free-free emission (Gillett et al. 1967). This excess was soon identified as due to thermal dust emission. From the fact that PNs are descendants of AGB stars, Kwok (1982) predicted that the remaining circumstellar dust envelope from AGB stars should be commonly detectable in PNs. The predictions were confirmed by the *Infrared Astronomical Satellite* (IRAS) observations, where over 1000 PNs were detected (Pottasch et al. 1984). The relative contributions from the stellar, nebular free-bound (f-b) and free-free (f-f) components, and dust continuum emissions in PNs have

been analyzed by many researchers such as Zhang & Kwok (1991) and Hsia et al. (2014).

The faint structures around PNs in the visible have been studied in several surveys (e.g., Stanghellini et al. 1993; Corradi et al. 2003; Cohen et al. 2011). Comparing with the observations at optical wavelengths, IR observations are less likely to be affected by the interstellar extinction. Thus it is highly desirable to observe faint structures around PNs in the IR. Moreover, unlike IR emissions, optical emissions are dominated by ionized gas. Therefore, a comparison study between IR and optical images allow us to better understand the processes of dust and gas components. Recent IR surveys have revealed new structures surrounding PNs (Ramos-Larios & Phillips 2009; Zhang et al. 2012a,b), these results suggest that PNs may reveal different morphologies in the optical and IR. The *Wide-field Infrared Survey Explorer* (WISE) survey covers entire sky area and its sensitivity is 100 times higher than IRAS (Wright et al. 2010). Thus, this survey provides a useful tool for us to resolve PNs with higher sensitivities

(Benjamin et al. 2003; Churchwell et al. 2009) and detect weak emissions from extended structures of known PNs.

Evolved PNs represent the last stage of the dispersion of stellar material into the interstellar medium (ISM). Gurzadyan (1969) first suggested that the interaction between PN and the ISM can decelerate the nebula. The observational evidence of PN-ISM interaction was later reported by Jacoby (1981). The signs of PN-ISM interactions have been found to be common among evolved PNs (Borkowski et al. 1990). To search and investigate the nebula/ISM boundary of evolved PNs can provide significant clue to study the mass-loss history of these objects and the matter enhancement in the galaxy.

The PNs M 2–55 (PN G116.2+08.5, IRAS 23296+7005) and Abell 2 (PN G122.1–04.9, IRAS 00426+5741) were first discovered and identified as evolved PNs by R. Minkowski in 1947 and Abell (1955) according to their low surface brightnesses and large angular diameters (Abell 1966). Based on early imaging studies, these objects have been classified as an irregular PN (Felli & Perinotto 1979) for M 2–55 and an elliptical nebula (Hua 1988) for Abell 2, respectively. Although their angular sizes ($\sim 60''$) are relatively larger than most PNs ($\sim 10''$ – $30''$), they have rarely been paid attention in the past thirty years. After a keyword search in the astrophysics data system (ADS) for these objects, only four records were found in the literature. The distance determination of PNs has long been a difficult problem. Recently, trigonometric parallax data release (DR) of Gaia mission has induced an investigation of reliable distances for many PNs (Bailer-Jones et al. 2018), allowing us to evaluate the distances of these two PNs with a higher accuracy.

In this paper, we present the results of a multi-wavelength investigation for PNs M 2–55 and Abell 2 based on optical and mid-infrared (MIR) images taken from *Lulin One-meter Telescope* and *WISE* all-sky survey, respectively, aiming to investigate the natures of the two PNs and their PN-ISM interactions. In Section 2, we describe the observations and data reductions. The results of imaging and spectroscopic observations in the optical and MIR are presented in Section 3. An analysis of the properties of the sources by analyzing their spectral energy distributions (SEDs) are presented in Section 4. A discussion and conclusions are summarized in Section 5 and Section 6, respectively.

2 OBSERVATIONS AND DATA REDUCTION

2.1 LOT Narrow-band Imaging

Narrow-band Images of these nebulae were obtained from the *Lulin One-meter Telescope* (LOT) on the Lulin

Observatory of National Central University (NCU) on the nights of 2018 November 4 – 2019 November 16. The Lulin Compact Imager (LCI) Sophia 2048B camera with a 2048×2048 CCD was used. The CCD camera has a field of view (FOV) of $13.2' \times 13.2'$ with an angular resolution of $0.39''$. These PNs were observed with three narrow-band filters: [O III] ($\lambda_c = 5009 \text{ \AA}$, $\Delta\lambda = 30 \text{ \AA}$), H α ($\lambda_c = 6563 \text{ \AA}$, $\Delta\lambda = 30 \text{ \AA}$), and [N II] ($\lambda_c = 6584 \text{ \AA}$, $\Delta\lambda = 10 \text{ \AA}$). The total exposures ranged from 7200 to 31 800 s for each filter of the deep observations. We process all imaging data using the IRAF software package. Dark-current correction, bias subtraction, and flat-field calibration were performed. A summary of these observations is given in Table 1. The reduced [OIII], H α , and [NII] images of these nebulae are shown in Figures 1 and 2, respectively.

2.2 YFOSC Optical Spectra

The spectra of M 2–55 were obtained on the nights of 2018 December 02 – 03, with the *Lijiang 2.4 m* telescope of the Yunnan Astronomy Observatories of China. The *Yunnan Faint Object Spectrograph and Camera* (YFOSC) instrument and an E2V 2048×4608 CCD were used. The spectral dispersion of the spectra is $\sim 1.7 \text{ \AA pixel}^{-1}$. The seeing conditions varied from $1.7''$ and $2.3''$ during the observing runs. The wavelength coverage of spectroscopic observations is between 3600 and 7700 \AA . The aperture size of a slit is $5' \times 1.8''$ and it was set through the central region of this nebula oriented toward the N-S direction. The exposures ranged from 1800 to 11 700 s and then the signal-to-noise (S/N) ratios of > 75 for main nebula were produced.

The data were reduced by a standard procedure using the NOAO IRAF V2.16 software package, including background subtraction, flat-fielding, and debiasing. For flux calibration, three KPNO standard stars each night were observed. To improve the S/N ratio, the final spectrum of this nebula was produced using the spectra with individual exposures. The journal of spectroscopic observations is given in Table 2.

Gaussian line profile fitting is used for measuring the fluxes of line emissions of this object. The uncertainties of line fluxes are derived from the continuum noise level. If we consider the flux errors of the measurements, the characteristic uncertainties of line emissions are about $\sim 5\%$ – 37% .

2.3 WISE Infrared Observations

MIR images of these PNs were taken from the *WISE* all-sky survey. The WISE mission has imaged all sky with four bands at 3.4, 4.6, 12, and 22 μm (W1–W4). The angular resolutions of the images for these four bands are $6.1''$,

Table 1 Summary of Narrow-band Imaging Observations

Object	Observation Date	Filter	λ_c (Å)	$\Delta\lambda$ (Å)	Seeing (arcsec)	Exposure (s)
M 2–55	2018 Nov. 04	H α	6563	30	2.1	600×20
	2018 Nov. 05	H α	6563	30	1.7	1800×11
	2018 Nov. 07	[O III]	5007	30	2.3	1800×4
	2018 Nov. 07	[N II]	6584	10	2.6	1800×7
Abell 2	2018 Nov. 05	H α	6563	30	1.8	1800×7
	2018 Nov. 06	H α	6563	30	1.9	1800×5
	2018 Nov. 06	[O III]	5007	30	2.2	1800×5
	2019 Oct. 13	[O III]	5007	30	1.8	1800×5
	2019 Oct. 16	[N II]	6584	10	1.4	1800×4
	2019 Nov. 16	[N II]	6584	10	1.3	1800×6

Table 2 Summary of YFOSC Spectroscopic Observations

Object	Observation Date	Wavelength (Å)	Dispersion (Å pix ⁻¹)	Width of Slit (arcsec)	Integration Time (s)
M 2–55	2018 Dec. 02	3600 – 7400	1.7	1.8	1800×2
	2018 Dec. 03	3600 – 7400	1.7	1.8	2700×3

6.4'', 6.5'', and 12'', respectively. The data used in this paper were retrieved from the NASA/IPAC Infrared Science Archive (IRSA)¹.

We performed the aperture photometric measurements for these nebulae using the method described in Hsia & Zhang (2014). The fluxes measured from the WISE images of these PNs have been calibrated using the color correction presented in Wright et al. (2010). To estimate the flux uncertainties, the standard deviations of systematic errors and all flux measurements are adopted. The estimated flux errors of the measurements in four bands for all objects are about 8% for W1, 9% for W2, 7% for W3, and 8% for W4 channels, respectively.

3 RESULTS

3.1 Optical Morphology

3.1.1 Multipolar planetary nebula – M 2–55

The PN of M 2–55 is originally classified as a B-class nebula with symmetrical structures (Sabbadin & Perinotto 1981). Our *LOT* narrow-band images (H α , [O III], and [N II]) of the nebula (Fig. 1) clearly show that this object is a multipolar PN with a size of $\sim 67.6''$, which is larger than the size of 39'' measured from the optical image reported by Acker et al. (1992). The appearance of M 2–55 is similar to that of the young PN M 1–30 (see fig. 1 of Hsia et al. 2014) and can be related to the quadrupolar PN (Manchado et al. 1996). The main structure of this PN consists two bipolar lobes (labeled as $a - a'$ and $b - b'$) and they are intersecting approximately at the central region of this object as shown in the H α and [N II] images (Fig. 1).

From Figure 1, we can see that the edges of two bipolar lobes are sharp and they are prominent in the H α and [N II] images. The central region of this nebula is mainly dominated by [O III] emission, while the lobes are more obscure in the [O III] image compared to those seen in the H α and [N II] images. Several clumpy regions can be seen within the main nebula. These regions may be due to the projection of two interlaced lobes. We note that some ray-shaped structures and radial filaments pointing toward the outer regions can be seen in the deep H α image. They may be the result of shadows of the clumpy region in the main nebula. These features can also be seen in other nebulae such as NGC 40, NGC 3242, NGC 3918, NGC 7009, NGC 7026, and NGC 7662 (Corradi et al. 2004). The position angles (PAs) of two pairs of lobes ($a - a'$ and $b - b'$) are measured to be $PA = 146^\circ \pm 3^\circ$ and $42^\circ \pm 3^\circ$. We measured the sizes of two lobes by fitting the shapes of these features to deep H α image. Two pairs of bipolar lobes have approximately the same extent. The angular sizes of two bipolar lobes are measured to be $67.2'' \times 36.6''$ and $65.5'' \times 34.3''$ for lobes $a - a'$ and $b - b'$, respectively.

Adopting a distance of 691 pc for M 2–55 (Bailer-Jones et al. 2018), the extent size is $0.23 \text{ sec}\theta$ pc for lobe $a - a'$, where θ is the inclination angle. The expansion velocity is assumed to be 20.3 km s^{-1} with [O III] emission (Weinberger 1989), the derived kinematic age of this nebula is about $5500 \text{ sec}\theta$ yr. This estimation is in good agreement with the earlier suggestion that M 2–55 is an evolved PN (Satiō et al. 1999).

3.1.2 Arc-like structure discovered around M 2–55

The filamentary appearance of the halo as observational evidence can provide that the nebula interacts with high-

¹ <http://irsa.ipac.caltech.edu/frontpage/>

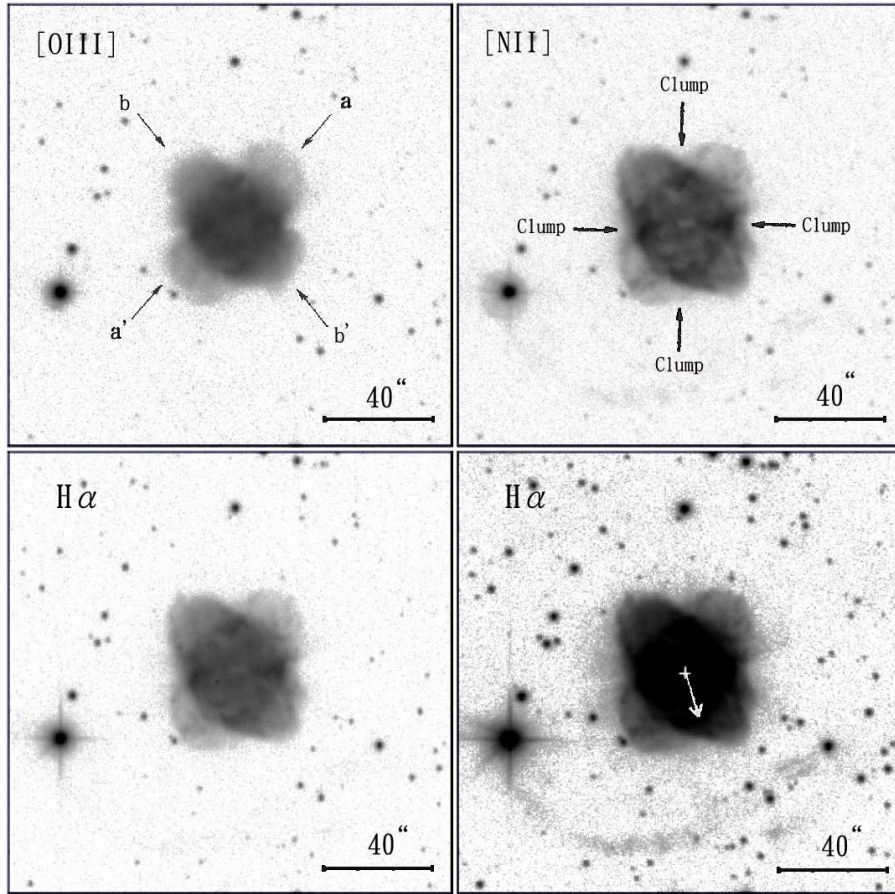


Fig. 1 Narrow-band images of M 2–55 in [O III] (*upper left*), [N II] (*upper right*), and H α (*lower left and lower right*) displayed with a logarithmic intensity scale. East is to the left and north is up. In the main nebula, two bipolar lobes (labeled as $a - a'$ and $b - b'$) and several clumps can be seen. Lower right panel: Same as on the lower-left panel but shown at different intensity levels. Outer extended filaments around this PN can be detected in the deep H α image. The position of the central star is marked with a cross. The white line denotes the direction of proper motion of this nebula.

density ISM (Dgani & Soker 1998; Ali *et al.* 2012). As a PN with low density moving through its surrounding ISM, the leading region of the halo is compressed and then the arc-like/bow-shock structure forms (Ali *et al.* 2012).

A new arc-like filament extending to $\sim 61''$ from the central star of this nebula can be seen in our deep H α image (see Fig. 1). The filamentary feature has not been detected in previous optical images. This arc shows a well-defined boundary from SW to SE, indicating that it may be a bow-shocked structure. The existence of this arc-shaped structure may suggest the PN-ISM interaction (Ramos-Larios *et al.* 2018; Wareing *et al.* 2007), which is supported by the proper motion direction of M 2–55 with PA = 192° (Roeser *et al.* 2010). The surface brightness (SB) profile of this filamentary feature with H α emission is shown in Figure 3. We made this profile from the average of the intervals between PA = 155° and PA = 185° , after removing all field stars. From Figure 3, the peak surface brightness of the arc-shaped structure (at the distance of $61''$ from the

central star) is $\sim 6 \times 10^{-2}$ times fainter than that of main nebula, and the feature is significantly brighter than the normal AGB halo (with a SB 10^{-3} times fainter than main shell; Corradi *et al.* 2003). Adopting a distance of 691 pc (Bailer-Jones *et al.* 2018) and assuming a typical expansion velocity of 13.7 km s^{-1} for this faint structure (Gussie & Taylor 1994), the observed size of this extended structure leads to a dynamical age of $\sim 15\,000$ yr. This suggests that the arc-like feature can be an important event of its AGB mass-loss history.

3.1.3 Double-shell planetary nebula – Abell 2

As can be seen in our narrow-band imaging, some structural features of PN Abell 2 show slightly different appearances which depends on the observed bands (Fig. 2). A close inspection of Figure 2 shows that two concentric elliptical shells (a brighter inner shell and a diffuse outer shell) are located in the main nebula. The limb-brightening

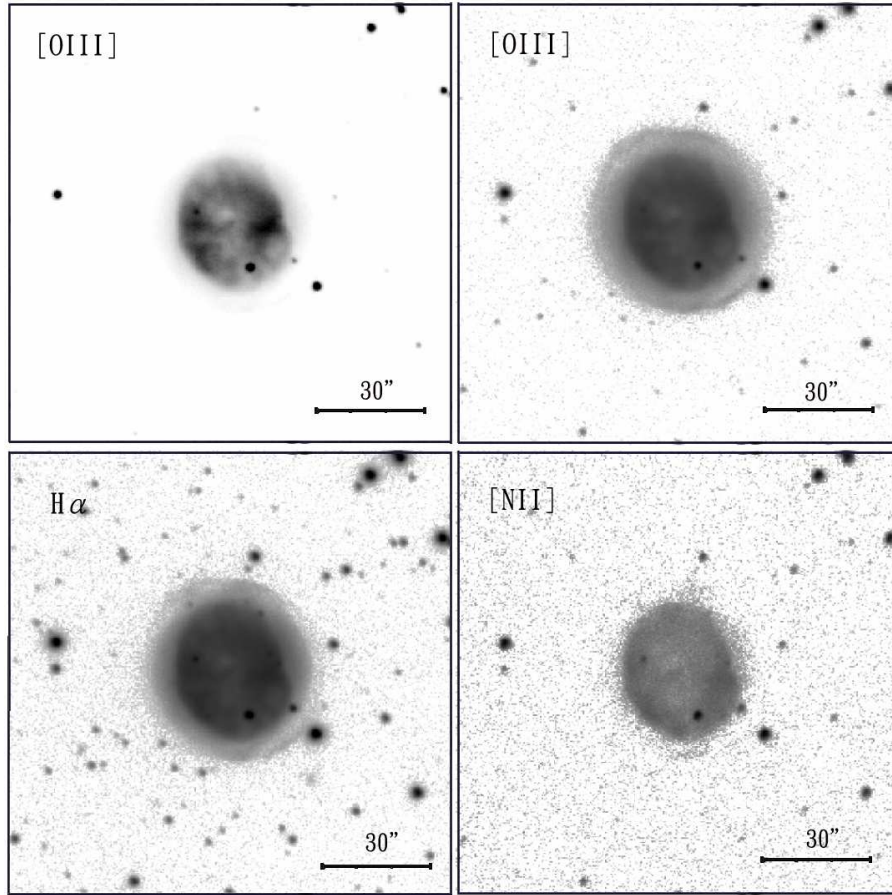


Fig. 2 (Upper left) Image of Abell 2 in [O III] displayed with a linear scale, where few clumpy structures can be seen in the inner shell. The [O III] (upper right), $H\alpha$ (lower left), and [N II] (lower right) images of this object are displayed on a logarithmic intensity scale to show the outer shell of the nebula. North is up and east is to the left.

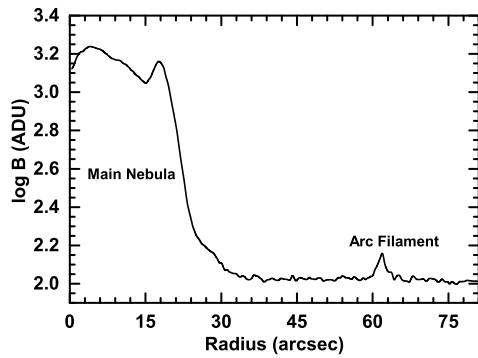


Fig. 3 $H\alpha$ surface brightness profile in M 2–55 averaged over the angles between $PA = 155^\circ$ and $PA = 185^\circ$. The horizontal axis is the distance from the central star in units of arcsec. The position of the arc-shaped structure is marked.

inner shell has a size of $\sim 37.4'' \times 31.2''$ and it is surrounded by a diffuse outer shell with a diameter of $\sim 52.3'' \times 47.6''$, which is larger than previously reported size of $35'' \times 35''$ (Hua 1988). The major axes of these shells are oriented

along $PA = 33^\circ$. From Figure 2, we can see that the inner elliptical shell with a clear boundary is prominent in $H\alpha$, [O III], and [N II] emissions, whereas the outer shell is undetectable in [N II]. These results suggest that the inner shell of this nebula is relatively lower excitation and outer diffuse shell farther away is relatively higher excitation, which is unusual among common PNs (Guerrero et al. 2018). Inside the inner shell of this nebula, a few small structural components can be seen in the [O III] and $H\alpha$ images. The origin and formation of these features are still unclear. It is possible that these features are produced from ionized non-uniform dense clumps. For this PN, the averaged value of nebular minor and major axial lengths as its size was adopted. At a distance of 2.82 kpc (Bailer-Jones et al. 2018), the average nebular size of this source is 0.68 pc, we obtained the dynamical age of $\sim 9\,800$ yr. Assuming an expansion velocity of the nebula is 34 km s^{-1} (Acker et al. 1992). This suggests that this nebula is indeed an old PN (Abell 1966; Hua 1988).

3.2 Extended Dust Halos around M 2–55 and Abell 2

To study the dust distributions and their properties of PNs M 2–55 and Abell 2, we have analyzed the MIR images of these nebulae retrieved from the *WISE* all-sky survey archive. The extended halos with IR emission surrounding the objects can clearly be seen in Figure 4. The MIR images show that the colors of the field stars are bluer than those of the nebulae, which suggests that they are dusty. The halos are detectable at *WISE* 12 and 22 μm bands, and they are brighter in the 22 μm images compared to the 12 μm images for these nebulae. Assuming that their emission peaks at 22 μm , we infer that IR fluxes emitted from the halos of these PNs are mainly dominated by dust components with a temperature of ~ 130 K. From Figure 4, we also note that PN M 2–55 shows lower IR surface brightness compared to PN Abell 2. In the *WISE* 12 and 22 μm images, the central parts of these nebulae show prominent IR emissions, probably suggesting a large amount of dust located in the central regions of these PNs although the emissions of [Ne V] $\lambda 24.3$ μm and [O IV] $\lambda 25.89$ μm may partly contribute to the fluxes of 22 μm band emissions (Chu et al. 2009).

The *WISE* color composite image of M 2–55 (left panel of Fig. 4) clearly shows that this PN has a slightly elliptical central nebula and an extended outer halo. The morphology of this nebula in the IR is different from that observed in the *LOT* optical narrow-band images. In this image, the central nebula is the brightest feature of this object, whereas the outer halo is 2×10^{-2} fainter. The southern part of the halo exhibits a well-defined boundary (with a size of $\sim 166''$), in contrast to a diffuse structure seen in the northern part of the halo. Such morphology gives an indication that this source is moving roughly toward the south and probably shows the PN-ISM interaction (Ramos-Larios & Phillips 2009; Zhang et al. 2012b). For Abell 2, the optical and MIR morphologies of this object are similar. Our MIR image (right panel of Fig. 4) shows an almost round halo with an angular diameter of $\sim 92''$. The central elliptical-shaped nebula is prominent in all *WISE* IR images. No evidence of related extended structure is found outside the halo of this object.

3.3 Spectral Properties of M 2–55

In order to understand the spatial distributions of extended arc-shaped structures with $\text{H}\alpha$ emission around PN M 2–55 (see Fig. 1), we have carried out spectroscopic observations. However, the faint filamentary feature is undetectable in our spectroscopic observations due to its low surface brightness compared to main shells of this PN (see

Table 3 Characteristic Lines in M 2–55

λ_{obs} (\AA) (1)	Identification		Observed Flux ^a (4)	Dereddened Flux ^a (5)
	λ_{lab} (\AA) (2)	Ion (3)		
4685.54	4685.68	He II	4.41 (16.5)	11.39 (16.5)
4860.74	4861.33	H β	16.81 (5.4)	37.78 (5.4)
4958.45	4958.91	[O III]	44.45 (13.8)	96.30 (13.8)
5006.31	5006.84	[O III]	137.91 (7.8)	289.80 (7.9)
5874.36	5875.66	He I	2.35 (13.6)	3.10 (13.7)
6300.03	6300.34	[O I]	2.20 (18.5)	2.43 (18.5)
6364.57	6363.78	[O I]	1.11 (36.7)	1.19 (36.7)
6547.04	6548.10	[N II]	17.24 (13.9)	17.34 (13.9)
6562.34	6562.77	H α	100.00 (3.2)	100.00 (3.2)
6582.81	6583.50	[N II]	56.56 (4.7)	56.12 (4.7)
6679.13	6678.16	He I	2.76 (5.4)	2.64 (5.4)
6716.07	6716.44	[S II]	4.60 (3.7)	4.35 (3.7)
6730.39	6730.82	[S II]	3.73 (7.6)	3.51 (7.6)
7178.15	7177.50	He II	6.39 (5.0)	5.17 (5.0)
7280.68	7281.35	He I	1.22 (11.1)	0.96 (11.1)
7299.17	7298.04	He I	1.59 (8.9)	1.24 (8.9)
7321.46	7319.99	[O II]	3.07 (7.1)	2.38 (7.1)

^a The normalized emission fluxes ($\text{H}\alpha = 100$). The brackets represent the flux uncertainty errors with percentage.

Sect. 3.1.2). Nevertheless, the properties of the main nebula can still be studied from our spectra.

The YFOSC spectrum of PN M 2–55 is shown in Figure 5. From Figure 5, we can see that a number of emission lines are typical in PN spectra. Among the prominent emission lines detected are H β at 4861 \AA , H α at 6563 \AA , [O III] at 4959, 5007 \AA , [N II] at 6548, 6584 \AA , and [S II] at 6717, 6731 \AA . Some weak emission features such as He I $\lambda\lambda 5876, 6678, 7281, 7298$, He II $\lambda\lambda 4686, 7178$, [O I] $\lambda\lambda 6300, 6364$, and [O II] $\lambda\lambda 7320$ can also be seen. The $N(\text{He})/N(\text{H})$ and $\log N/\text{O}$ ratios (Peimbert & Torres-Peimbert 1983) suggest that the nebula is a type I PN (Peimbert & Torres-Peimbert 1983, 1987), which is believed to originate from a massive progenitor star (Calvet & Peimbert 1983; Kingsburgh & Barlow 1994). The $\text{H}\alpha/\text{H}\beta$ flux ratio measured from M 2–55 is 5.95 ± 0.48 . Given the theoretical values at $T_e = 10^4$ K and $n_e = 10^2 \text{ cm}^{-3}$ (Hummer & Storey 1987), the extinction value of $c = 1.13 \pm 0.13$ is derived by comparing the observed $\text{H}\alpha/\text{H}\beta$ ratio and using the reddening law with a $R_V = 3.1$ (Howarth 1983). This extinction is in good agreement with the earlier reported value of $c = 1.24$ (Kaler et al. 1990).

The measured emission fluxes are given in Table 3. Columns (1)–(3) list the observed emission wavelengths and line identifications. The normalized measured and dereddened fluxes ($\text{H}\alpha = 100$) of this object are listed in Columns (4) and (5). The observed integrated H β flux measured from this PN is $3.73 \times 10^{-14} \text{ erg cm}^{-2} \text{ s}^{-1}$. From Table 3, the line ratios of [O III] $\lambda 5007/\lambda 4959$ and [N II] $\lambda 6584/\lambda 6548$ of this nebula are 3.0 and 3.2, respectively, which are consistent with the theoretical values suggested

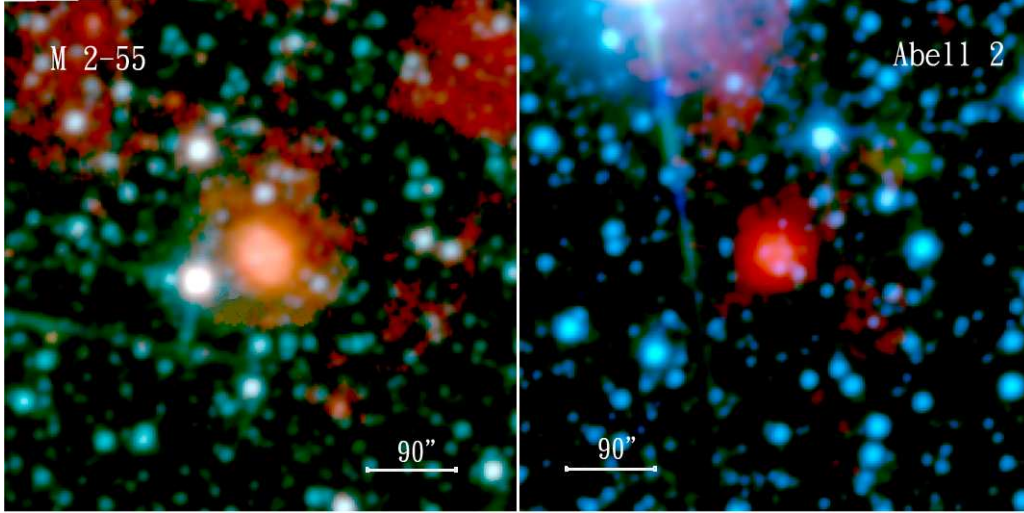


Fig. 4 Color composite *WISE* images of M 2–55 and Abell 2. The infrared images are shown on a logarithmic scale. These PNs are made from three bands: 3.4 μm (shown as *blue*), 4.6 μm (*green*), and 22 μm (*red*). North is up and east is to left. The extended halos around these PNs can be seen in the images.

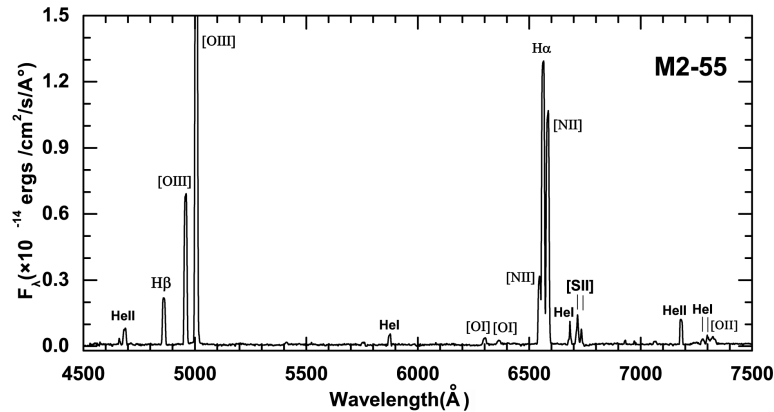


Fig. 5 Optical spectrum of M 2–55 in the wavelength range of 4500 \AA to 7500 \AA . The prominent emission features are marked.

by Storey & Zeppen (2000). Adopting an electron temperature of $T_e = 10\,200$ K (Peimbert & Torres-Peimbert 1987) for this nebula and using the $[\text{S II}] \lambda 6731/\lambda 6717$ line ratio, the electron density $n_e = 250_{-190}^{+210} \text{ cm}^{-3}$ was derived. This value is in good agreement with the earlier results of 460 cm^{-3} (Peimbert & Torres-Peimbert 1987) and 512 cm^{-3} (Phillips 1998). The slight difference stems from different diaphragm sizes and slit positions. The emission ratio of $\log([\text{O III}] \lambda 5007 + \lambda 4959/\text{He II} \lambda 4686)$ is a useful probe to determine the excitation class of a PN (Gurzadyan 1988). For this object, the value of $\log([\text{O III}] \lambda 5007 + \lambda 4959/\text{He II} \lambda 4686)$ ratio is about 1.53, which indicates that this nebula is a high-excitation class PN. Moreover, the $\text{H}\alpha/[\text{O III}] \lambda 5007$ flux ratio of M 2–55 is 0.35, which is smaller than that of normal young PNs (>1.5 ; Sahai & Trauger 1998), suggesting that this object is evolved.

4 SPECTRAL ENERGY DISTRIBUTION

To understand the properties of the ionized gas, photospheric, and dust components of these objects, the SEDs for PNs M 2–55 and Abell 2 were constructed (Figs. 6 and 7). In the IR, the Infrared Space Observatory (ISO) Long Wavelength Spectrometer (LWS) spectrum was used. For photometric measurements, the near-ultraviolet (NUV) and optical B , V , i , z , and y photometry of these objects are obtained from Shaw & Kaler (1985), Martin et al. (2005), Zacharias et al. (2005), and Chambers et al. (2016). J , H , and K_s band photometric data are taken from *Two Micron All Sky Survey* (2MASS) database. In the MIR, we used the data from *AKARI* and *IRAS* Source catalogs. In addition, the photometric data of these PNs measured from *WISE* MIR images are also added. A summary of these data used is given in Table 4.

Table 4 Photometric Measurements of M 2–55 and Abell 2

Filters	M2–55		Abell 2	
	Flux/Flux density	Reference	Flux/Flux density	Reference
Central star and nebula				
Galex NUV (mag)	17.59±0.04	Martin et al. (2005)
<i>B</i> (mag)	17.43	Zacharias et al. (2005)	16.07±0.30	Shaw & Kaler (1985)
<i>V</i> (mag)	15.85±0.20	Shaw & Kaler (1985)
Pan-Starrs <i>i</i> (mag)	16.36±0.01	Chambers et al. (2016)
Pan-Starrs <i>z</i> (mag)	16.01±0.01	Chambers et al. (2016)
Pan-Starrs <i>y</i> (mag)	15.75±0.01	Chambers et al. (2016)
Dust ^a				
2MASS <i>J</i> (mag)	14.57±0.04	Cutri et al. (2003)
2MASS <i>H</i> (mag)	13.75±0.05	Cutri et al. (2003)
2MASS <i>K_s</i> (mag)	13.56±0.05	Cutri et al. (2003)
WISE 3.4 μm (mag)	11.43±0.03	this study	12.92±0.02	this study
WISE 4.6 μm (mag)	10.13±0.02	this study	12.34±0.03	this study
WISE 12 μm (mag)	6.83±0.02	this study	8.35±0.04	this study
WISE 22 μm (mag)	3.75±0.03	this study	5.05±0.03	this study
IRAS 12 μm ^b (Jy)	0.49:	Tajitsu & Tamura (1998)	0.11:	Tajitsu & Tamura (1998)
IRAS 25 μm (Jy)	0.80±0.07	Tajitsu & Tamura (1998)	0.14±0.02	Tajitsu & Tamura (1998)
IRAS 60 μm (Jy)	3.55±0.28	Tajitsu & Tamura (1998)	0.65±0.13	Tajitsu & Tamura (1998)
IRAS 100 μm ^b (Jy)	4.99±0.40	Tajitsu & Tamura (1998)	7.77:	Tajitsu & Tamura (1998)
AKARI 65 μm (Jy)	1.85:	Yamamura et al. (2010)
AKARI 90 μm (Jy)	3.76±0.16	Yamamura et al. (2010)	0.67±0.08	Yamamura et al. (2010)
AKARI 140 μm (Jy)	3.58±0.63	Yamamura et al. (2010)	0.01:	Yamamura et al. (2010)
AKARI 160 μm (Jy)	1.76:	Yamamura et al. (2010)	0.33:	Yamamura et al. (2010)
Free-free emission				
5 GHz (mJy)	19	Siódmiak & Tylenda (2001)	2.3	Stanghellini et al. (2008)
4.85 GHz (mJy)	28±4	Gregory et al. (1996)
1.4 GHz (mJy)	26.6	Siódmiak & Tylenda (2001)	7.6±0.6	Condon et al. (1998)
1.4 GHz (mJy)	9.4±1.1	Condon & Kaplan (1998)

^a The colons represent the uncertain flux measurement. ^b Some IRAS 12 and 100 μm fluxes are upper limit detections.

The preliminary impression of the SEDs (Figs. 6 and 7) is that most of the fluxes from these PNs are mainly dominated in the IR. Assuming that the dust emission can be represented by a single blackbody (BB), the peak fluxes of these SEDs are 8.5×10^{-10} erg cm⁻² s⁻¹ and 1×10^{-10} erg cm⁻² s⁻¹ for M 2–55 and Abell 2, and the total fluxes emitted from the objects are approximately 1.2×10^{-9} erg cm⁻² s⁻¹ for M 2–55 and 1.4×10^{-10} erg cm⁻² s⁻¹ for Abell 2. Adopting their distances of 691 pc and 2.82 kpc for M 2–55 and Abell 2 (Bailer-Jones et al. 2018), the total luminosity of these nebulae are about 18 and 35 L_{\odot} for M 2–55 and Abell 2, respectively. From Figures 6 and 7, we note that the IR SED of each PN cannot be fitted by a single BB, thus these derived values are just the minima.

We fitted the emerging fluxes of these objects by a two-component model including the reddened photospheric emission (emitted from the central star and gaseous emission) and dust continuum using the same expressions described in Hsia et al. (2019). The mid- to far-infrared component of the SED is not fitted by a single dust component. We have tried to fit the observed SED by a radiation transfer model using the software code DUSTY (Ivezic et al. 1999). For the fitting, we assumed the stan-

dard MRN distribution of grain sizes (Mathis et al. 1977) with a dust temperature on the inner shell boundary of 90 K and a density distribution of R^{-2} for each object, where R is the distance to the central star. In order to arrive at the best fitting, the optical thicknesses of the shells at 0.55 μm were adopted to be $\tau = 3$ and $\tau = 0.6$ for M 2–55 and Abell 2. The dust grains are assumed to be the mixings of silicates and graphite, which can give the approximations to the dust continua. The separated contributions from different components of these PNs can be clearly seen in Figures 6 and 7. For the SED fittings, our best estimates for the central star temperatures are 80 000 K for M 2–55 and 78 000 K for Abell 2, which are in good agreement with previously results of 85 000 K (Kaler & Jacoby 1989) and $75\,000 \pm 4000$ K (Shaw & Kaler 1985) for M 2–55 and Abell 2. With the adopted distances of 691 pc for M 2–55 and 2.82 kpc for Abell 2 (Bailer-Jones et al. 2018), the derived total luminosity of the objects are about 35 and 50 L_{\odot} for M 2–55 and Abell 2, respectively, which are higher than our earlier estimates because parts of UV radiation emitted from the central stars are not counted in the total observed fluxes. The higher central star temperatures and low luminosities of these PNs indicate that they are on the cooling paths of their evolutions

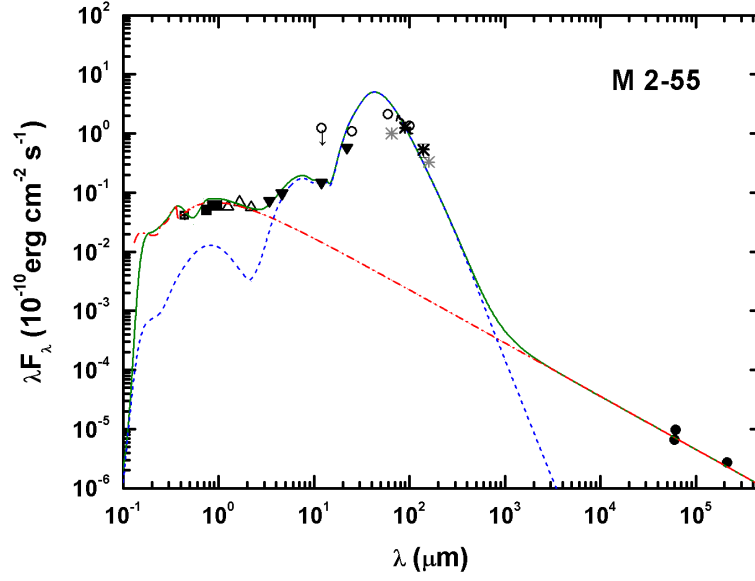


Fig. 6 The SED of M 2–55 with wavelength range from UV to radio. The Pan-Starrs measurements are shown as *filled squares*, the NUV, *B*, and *V* measurements as *open squares*, the 2MASS results as *open triangles*, WISE measurements as *filled triangles*, IRAS as *open circles*, AKARI photometry as *asterisks*, and radio measurements as *filled circles*. The uncertain AKARI detections are marked as the *light asterisks*. Note that the measured IRAS 12 and 100 μm fluxes are upper limit detections. The ISO LWS spectrum for M 2–55 is also plotted. The nebular emissions are plotted as the *red curve*. The *blue curve* represents a dust continuum fitting by using the radiation transfer model. The total fluxes derived from all components are plotted as the *green curve*.

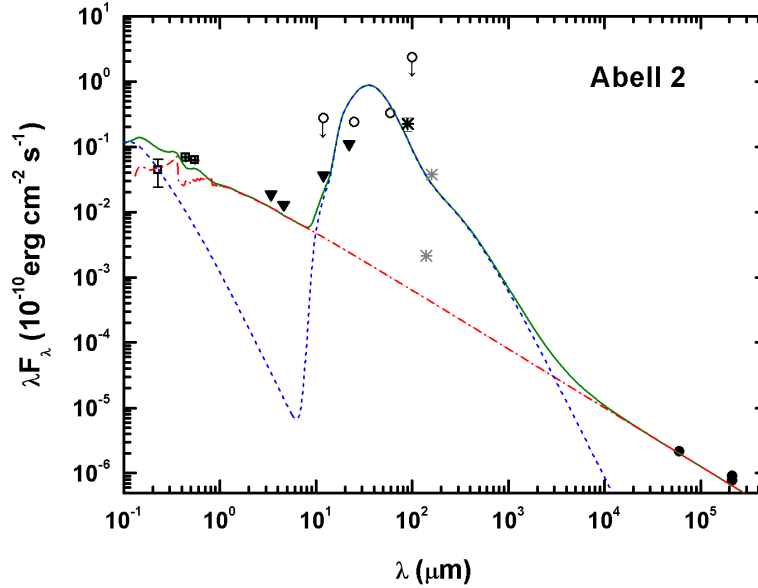


Fig. 7 The SED of Abell 2 with the spectral range from 1000 \AA to 50 cm. The notations of data points and fitting curves are the same as Fig. 6.

in the Hertzsprung-Russell (H-R) diagram. Using the formulas presented in Hsia et al. (2010), we can derive the mass of dust component (M_d) and the mass of ionized gas (M_i) of PN M 2–55. Assuming the emissivity of dust particles of $Q_\lambda = Q_0(\lambda/\lambda_0)^{-\alpha}$, where $Q_0 = 0.1$, $\alpha = 1$, and $\lambda_0 = 1 \mu\text{m}$. The assumed density of dust grains of

$\rho_s = 1 \text{ g cm}^{-3}$ and the adopted distance of 691 pc, we obtain $4.01 \times 10^{-4} M_\odot$ and $1.1 \times 10^{-2} M_\odot$ for the masses of the dust component (M_d) and ionized gas (M_i), respectively. The M_d/M_i ratio of M 2–55 is ~ 0.04 , significantly higher than the dust-to-gas ratios of typical PNs ($10^{-2} - 10^{-3}$, Stasińska & Szczerba 1999). This proba-

bly suggests that a mass of gas in this evolved PN is in neutral form.

5 DISCUSSION

5.1 M 2–55

According to Tweedy & Kwitter (1996) and Dgani & Soker (1998), the interacting PNs show three distinct features of the interactions with their surrounding ISM; (i) the outer regions around the PNs are asymmetric; (ii) brightness enhancements seen in the outer regions of these PNs accompanied by the drops in the ionization levels; (iii) the presences of fragments in the halos and/or arc-shaped filaments. Dgani & Soker (1998) suggested that the striped appearances of interacting PNs may be the result of Rayleigh-Taylor (RT) instabilities, resulting in fragmentations at the halos of the PNs. The optical-infrared morphology of PN M 2–55 as seen in Figures 1 and 4 is composed of an arc-like structure with brightness enhancement on its edge from SW to SE (see Sect. 3.1.2) and an asymmetric infrared halo (see Sect. 3.2). Such features have been detected in other nebulae such as NGC 6751 (Clark et al. 2010), NGC 6894 (Soker & Zucker 1997), NGC 7293 (Zhang et al. 2012b), HW 4, S176, and S188 (Tweedy & Kwitter 1996), and have been attributed to the interactions between the AGB winds and the ISM. No evidence of the other two distinct characteristics of PN-ISM interactions can be seen in this object. We conclude that the presence of the arc-shaped structure seen around PN M 2–55 is caused by the compression from the motion of this nebula through its surrounding ISM.

Wilkin (1996) found that the arc-shaped structure depends on relative velocities and densities between slow AGB wind and the surrounding ISM, the presence of the feature can be used to determine the properties of AGB wind of the PN and its surrounding ISM. We note that the appearance of this newly discovered arc filament is similar to that of brightening structure as the first stage of PN-ISM interaction in the simulations of Wareing et al. (2007), probably suggesting that the PN is not affected by the ISM interaction. If the central star of the planetary nebula (CSPN) moves slowly through the ISM (i.e., $< 50 \text{ km s}^{-1}$; Burton 1988), this interaction can remain for the entire lifetime of the nebula and other PN-ISM interactions will never be observed (Wareing et al. 2007). In the case of PN M 2–55, the radial velocity of this object is 22.6 km s^{-1} (Acker et al. 1992), hence we infer that the arc-shaped structure around this PN may be observed for a long time.

Although M 2–55 has been known to present two pairs of bipolar lobes (Sabbadin & Perinotto 1981), previous im-

ages did not reveal internal details of this nebula. Figure 1 shows that the nebular structures are point symmetric about the center, and the two pairs of lobes have approximately the same extent, indicating that they were ejected during a short period. This PN also reveals a large central cavity, differing from young bipolar PNs which usually exhibit a narrow waist (see, e.g., Manchado et al. 1996; Kwok & Su 2005). Presumably, the central cavity was created by the increasing thermal pressure with PN evolution. The clumpy structures in Figure 1 might be the debris of the torus that have collimated the outflows. A hypothesis of PN evolutionary transition from bipolar (lobe-dominant) to elliptical (cavity-dominant) has been suggested by Huarte-Espinosa et al. (2012) and Hsia et al. (2014). The appearance of PN M 2–55 suggests that it is in an evolutionary stage between the lobe-dominant phase and the cavity-dominant phase.

5.2 Abell 2

According to the evolutionary tracks presented in Blöcker (1995), the temperature and luminosity of the central star of Abell 2 indicate that it has a mass of $\sim 0.605 M_{\odot}$. This is normal among PNs (Stasińska et al. 1997). Soker (1997) classified Abell 2 as an elliptical PN, which might result from axisymmetric mass loss of its progenitor interacted with a substellar companion during the common envelope phase. This scenario also predicts the existence of a spherical halo surrounding elliptical nebula (Soker 1997), which is confirmed by our observation of Abell 2 (see Sect. 3.2).

The hydrodynamical models presented by Gawryszczak et al. (2002) suggest that PNs with binary cores will evolve from bipolar to elliptical shapes. Therefore, elliptical PNs can be produced in wide binary systems and most evolved PNs appear spherical or elliptical morphologies. This results from the possibility that there is a companion in the nucleus of Abell 2. Although our observations could not identify whether a companion exists in this PN, new spectroscopic observation is required to reveal the nature of the nucleus in Abell 2.

The double-shell structure of Abell 2 can be explained in terms of radiation-hydrodynamics simulations (Schönberner et al. 2014). Similar to the PN double-shell HuBi 1 (Guerrero et al. 2018), the inner and outer shells of Abell 2 appears to have an opposite ionization structure to those of typical PNs. Guerrero et al. (2018) suggested that the anomalous excitations are related the Wolf-Rayet central star of the PN. In this case, the nucleus of the nebula may experience a born-again event produced by a thermal pulsation at the ending of AGB stage, during the post-AGB phase (Blöcker 2001), or on the cooling stage of white dwarf evolution (Schönberner 1979). The shocks produced

by the ejecta excite the inner shell, resulting in an inverted ionization structure as seen in Abell 2.

It is instructive to investigate the evolution of SEDs from young to old PNs. The SED of a young PN IRAS 21282+5050 (hereafter referred to as IRAS 21282) has been presented by Hsia et al. (2019), whether a strong IR excess due to thermal emission of dust components has been revealed. In IRAS 21282, the dust envelope is optically thick with an optical depth of $\tau = 5.5$ at $0.55 \mu\text{m}$, and has a high temperature of $\sim 250 \text{ K}$. It is clear that the evolved PN Abell 2 exhibits a lower optical depth and a lower temperature. Therefore, the infrared colors can reflect the evolutionary stage of PNs.

6 CONCLUSIONS

Recent narrow-band imaging studies have provided an effective tool for us to understand the ionized gaseous environments around evolved PNs. Although more than one hundred extended, faint PNs have been studied via these advanced observational tools (Tweedy & Kwitter 1996; Corradi et al. 2003; Ali et al. 2012), the nature and properties of these nebulae are still unclear. In this paper, we present a visible and MIR study of two evolved PNs (M 2–55 and Abell 2). Our deep optical narrow-band images of PN M 2–55 reveal two pairs of bipolar lobes and a new arc-like structure. The arc-shaped structure seen around this object appears as a well-defined boundary from SW to SE, furnishing strong evidence for an interaction of the expanding nebula of this PN with its surrounding ISM. The [O III] and $\text{H}\alpha$ images of PN Abell 2 reveal inner and outer elliptical shells in the main nebula, whereas the inner shell of this PN can only be seen in the [N II] image. This suggests that the nucleus of this PN experienced a born-again event. We have studied the nebular properties of PN M 2–55 by the mid-resolution spectrum. The spectral analysis of this object shows that the nebula is an evolved PN with a high excitation class and a low electron density of 250 cm^{-3} .

From the MIR images of *WISE* all-sky survey data release, these PNs presented in our study are found to show prominent infrared features. Obvious MIR emissions detected in the central parts of these objects suggest that a mass of dust is located in their central regions. The SEDs of these PNs are constructed from extensive archival data. We successfully fitted the observed fluxes by a two-component model including the reddened photospheric emission and dust continuum. These PNs might have thick dusty envelopes because most of the fluxes from the objects are emitted by dust components.

Interacting PN is thought to be the result of dynamical interaction between slow AGB wind (halo) and its surrounding ISM. The presence of arc-shaped/bow-shock

structure suggests that PN-ISM interaction may be very common. M 2–55 and Abell 2 can serve as an astrophysical laboratory to study the dynamical processes of the interactions between PNs and ISM in the space.

Acknowledgements We would like to thank the anonymous referee for his/her helpful comments that improved the manuscript. This publication has made use of data collected at the Lulin Observatory, partly supported by MoST grant (108-2112-M-008-001). We acknowledge the support of the staff of the Lijiang 2.4m telescope. Funding for the telescope has been provided by Chinese Academy of Sciences and the People’s Government of Yunnan Province. Financial support for this work is supported by the grants from The Science and Technology Development Fund, Macau SAR (file no: 061/2017/A2 and 0007/2019/A) and the Faculty Research Grants of Macau University of Science and Technology (project code: FRG-19-004-SSI). X.L. is supported by the National Natural Science Foundation of China (NSFC, Grant No. U1731122). Y.Z. thanks NSFC (Grant No. 11973099) for financial support.

References

- Abell, G. O. 1955, *PASP*, 67, 258
- Abell, G. O. 1966, *ApJ*, 144, 259
- Acker, A., Ochsenbein, F., Stenholm, B., et al. 1992, *Strasbourg-ESO Catalog of Galactic Planetary Nebulae, Parts I and II* (Garching: European Southern Observatory)
- Ali, A., Sabin, L., Snaid, S., & Basurah, H. M. 2012, *A&A*, 541, A98
- Bailer-Jones, C. A. L., Rybizki, J., Fouesneau, M., et al. 2018, *AJ*, 156, 58
- Benjamin, R. A., Churchwell, E., Babler, B. L., et al. 2003, *PASP*, 115, 953
- Blöcker, T., 1995, *A&A*, 299, 755
- Blöcker, T., 2001, *Ap&SS*, 275, 1
- Borkowski, K. J., Sarazin, C. L., & Soker, N. 1990, *ApJ*, 360, 173
- Burton, W. B., 1988, in *Galactic and Extragalactic Radio Astronomy*, eds. K. Kellermann, & G. L. Verschuur (New York: Springer), 295
- Calvet, N., & Peimbert, M. 1983, *Rev. Mexicana Astron. Astrofis.*, 5, 319
- Chambers, K. C., Magnier, E. A., Metcalfe, N., et al. 2016, arXiv e-prints, arXiv:1612.05560
- Chu, Y. -H., Gruendl, R. A., Guerrero, M. A., et al. 2009, *AJ*, 138, 691
- Churchwell, E., Babler, B. L., Meade, M. R., et al. 2009, *PASP*, 121, 213
- Clark, D. M., García-Díaz, Ma. T., López, J. A., et al. 2010, *ApJ*, 722, 1260

- Condon, J. J., Cotton, W. D., Greisen, E. W., et al. 1998, *AJ*, 115, 1693
- Condon, J. J., & Kaplan, D. L. 1998, *ApJS*, 117, 361
- Cohen, M., Parker, Q. A., Green, A. J., et al. 2011, *MNRAS*, 413, 514
- Corradi, R. L. M., Schönberner, D., Steffen, M., et al. 2003, *MNRAS*, 340, 417
- Corradi, R. L. M., Sánchez-Blázquez, P., Mellema, G., et al. 2004, *A&A*, 417, 637
- Cutri, R. M., Skrutskie, M. F., van Dyk, S., et al. 2003, *VizieR Online Data Catalog*, II/246
- Dgani, R., & Soker, N. 1998, *ApJ*, 495, 337
- Felli, M., & Perinotto, M. 1979, *A&A*, 76, 69
- Gawryszczak, A. J., Mikołajewska, J., & Różyczka, M. 2002, *A&A*, 385, 205
- Gillett, F. C., Low, F. J., & Stein, W. A. 1967, *ApJ*, 149, L97
- Gregory, P. C., Scott, W. K., Douglas, K., et al. 1996, *ApJS*, 103, 427
- Guerrero, M. A., Fang, X., Miller Bertolami, M. M., et al. 2018, *Nature Astronomy*, 2, 784
- Gurzadyan, G. A. 1969, *Planetary Nebulae* (New York: Gordon & Breach)
- Gurzadyan, G. A. 1988, *Ap&SS*, 149, 343
- Gussie, G. T., & Taylor, A. R. 1994, *PASP*, 106, 500
- Howarth, I. D. 1983, *MNRAS*, 203, 301
- Hsia, C. -H., Kwok, S., Zhang, Y., et al. 2010, *ApJ*, 725, 173
- Hsia, C. -H., Chau, W., Zhang, Y., et al. 2014, *ApJ*, 787, 25
- Hsia, C. -H., & Zhang, Y. 2014, *A&A*, 563A, 63
- Hsia, C. -H., Zhang, Y., Kwok, S., et al. 2019, *Ap&SS*, 364, 32
- Hua, C. T. 1988, *A&A*, 193, 273
- Huarte-Espinosa, M., Frank, A., Balick, B., et al. 2012, *MNRAS*, 424, 2055
- Hummer, D. G., & Storey, P. J. 1987, *MNRAS*, 224, 801
- Ivezic, Z., Nenkova, M., & Elitzur, M. 1999, *User Manual for Dusty* (University of Kentucky) eprint arXiv:astro-ph/9910475
- Jacoby, G. H. 1981, *AJ*, 244, 903
- Kaler, J. B., & Jacoby, G. H. 1989, *ApJ*, 345, 871
- Kaler, J. B., Shaw, R. A., & Kwitter, K. B. 1990, *ApJ*, 359, 392
- Kingsburgh R. L., & Barlow M. J. 1994, *MNRAS*, 271, 257
- Kwok, S. 1982, *ApJ*, 258, 280
- Kwok, S., & Su, K. Y. L. 2005, *ApJ*, 635, 49
- Manchado, A., Stanghellini, L., & Guerrero, M. A. 1996, *ApJ*, 466, 95
- Martin, D. C., Fanson, J., Schiminovich, D., et al. 2005, *ApJ*, 619, L1
- Mathis, J. S., Ruml, W., & Nordsieck, K. H. 1977, *ApJ*, 217, 425
- Peimbert M. & Torres-Peimbert S. 1983, *IAU Symp.* 103, Reidel, Dordrecht, 233
- Peimbert M. & Torres-Peimbert S. 1987, *Rev. Mexicana Astron. Astrofis.*, 14, 540
- Phillips, J. P. 1998, *A&A*, 340, 527
- Pottasch, S. R., Baud, B., Beintema, D., et al. 1984, *A&A*, 138, 10
- Ramos-Larios, G., & Phillips, J. P. 2009, *MNRAS*, 400, 575
- Ramos-Larios, G., Guerrero, M. A., Nigoche-Netro, A., et al. 2018, *MNRAS*, 475, 932
- Roeser, S., Demleitner, M., & Schilback, E. 2010, *AJ*, 139, 2440
- Sabbadin, F., & Perinotto, M. 1981, *A&A*, 94, 25
- Sahai, R., & Trauger, J. T. 1998, *AJ*, 116, 1357
- Satiō, M., Iwata, I., Okumura, S., Mori, A., & Yamashita, T. 1999, *PASJ*, 51, 673
- Schönberner, D., 1979, *A&A*, 79, 108
- Schönberner, D., Jacob, R., Lehmann, H., et al. 2014, *Astron. Nachr.*, 335, 378
- Shaw, R. A., & Kaler, J. B. 1985, *ApJ*, 295, 537
- Siódmiak, N., & Tylenda, R. 2001, *A&A*, 373, 1032
- Soker, N., 1997, *ApJS*, 112, 487
- Soker, N., & Zucker, D. B. 1997, *MNRAS*, 289, 665
- Stanghellini, L., Corradi, R. L. M., & Schwarz, H. E. 1993, *A&A*, 279, 521
- Stanghellini, L., Shaw, R. A., & Villaver, E. 2008, *ApJ*, 689, 194
- Stasińska, G., Górny, S. K. & Tylenda, R., 1997, *A&A*, 327, 736
- Stasińska, G., & Szczerba, R. 1999, *A&A*, 352, 297
- Storey, P. J. & Zeippen, C. J. 2000, *MNRAS*, 312, 813
- Tajitsu, A., & Tamura, S. 1998, *AJ*, 115, 1989
- Tweedy, R. W., & Kwitter, K. B. 1996, *ApJS*, 107, 255
- Wareing, C. J., Zijlstra, A. A., & O'brien, T. J. 2007, *MNRAS*, 382, 1233
- Weinberger, R. 1989, *A&AS*, 78, 301
- Wilkin, F. P. 1996, *ApJ*, 459, L31
- Wright, E. L., Eisenhardt, P. R. M., Mainzer, A. K., et al. 2010, *AJ*, 140, 1868
- Yamamura, I., Makiuti, S., Ikeda, N., et al. 2010, *VizieR Online Data Catalog*, 2298, 0
- Zacharias, N., Monet, D. G., Levine, S. E., et al. 2005, *VizieR Online Data Catalog*, 1297, 0
- Zhang, C. Y., & Kwok, S. 1991, *A&A*, 250, 179
- Zhang, Y., Hsia, C. -H., & Kwok, S. 2012a, *ApJ*, 745, 59
- Zhang, Y., Hsia, C. -H., & Kwok, S. 2012b, *ApJ*, 755, 53